Fluid Phase Equilibria 609 (2026) 114743

Contents lists available at ScienceDirect

Fluid Phase Equilibria

journal homepage: www.journals.elsevier.com/fluid-phase-equilibria

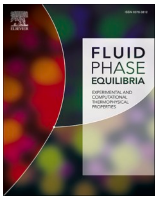

Electrolyte evaporation after an electrolyte leakage in a quiescent environment: a computational fluid dynamic study

Fabio Ferrario [a,b], Natalia Lebedeva [b,*], Valentina Busini [a,*]

[a] Department of Chemistry, Materials and Chemical Engineering "Giulio Natta", Politecnico di Milano, Milan, 20131, Italy
[b] Joint Research Centre, European Commission, Petten, the Netherlands

ARTICLE INFO

Keywords:
Lithium ion batteries
Electrolyte leakage
Evaporation model
Dispersion model
Heavy vapours
Computational fluid dynamics

ABSTRACT

The leakage of electrolyte from battery cells is one of the most common battery failure mechanisms and may lead to the release of harmful compounds to the general population. This is due to the high volatility and toxicity of common electrolyte solvents, such as dimethyl carbonate (DMC) and diethyl carbonate (DEC). Detection and early warning systems are therefore needed, particularly in enclosed and poorly ventilated environments such as garages.

In this work, a CFD-RANS evaporation and dispersion model was applied to simulate electrolyte leakage in an enclosed, non-ventilated garage, with the aim of assessing the optimal positioning of sensors for early leakage detection.

Results from the garage simulations of the evaporation and dispersion of pure DMC and DEC show that the generated vapours behave as heavy gases, spreading radially within the environment and accumulating near the source. Furthermore, large environments like the one presented in this work (50.7 m^3), where radial dispersion is favoured, severely limits vertical dispersion because it is obstacle-driven (*i.e.*, the vapour cloud interacts with walls earlier in smaller environments). A comparison between a simplified single-component evaporation approach and a full electrolyte approach was performed. The full electrolyte evaporation scenario predicted that dangerous concentrations of DMC that could lead to irreversible health effects (*i.e.*, Protection Action Criteria, PAC-2 = 120 ppm) may be reached at 15 cm from the ground at 45 min after leakage, while the pure DMC scenario predicted that PAC-2 concentrations were reached at 15 cm at 24 min after leakage. Therefore, the simplified single-component approach is not able to accurately reproduce the behaviour of the full electrolyte leakage scenario.

1. Introduction

One of the most pressing issues on a global scale is the increasing effect that climate change is having on the environment [1]. The constant release of greenhouse gases has significant consequences: from raising temperatures worldwide [2] to rising sea levels [3], concern for the future has led many countries to support the green energy transition [4]. Transitioning to low-carbon power sources, like wind and solar, can help limit the release of harmful compounds and slow down climate change. In the last few years, lithium-ion batteries (LIBs) have become a key-enabling technology for the energy transition, for both the mobility and energy storage sectors [5]. This is due to their high energy density, high cycle stability, and fast charging capability, compared to conventional rechargeable battery technologies such as lead–acid and nickel-based batteries, making LIBs an efficient and cost-effective solution for energy storage [6,7].

While LIBs are generally a safe and reliable technology when used within their operating parameters, recent reports of battery-related fires [8,9] has started an industry-wide effort to address safety issues that LIB technology may have. Critically, thermal runaway reactions may result in fire generation due to mechanical abuse [10], battery ageing [11], or electrolyte leakage, which may lead to the deterioration of the battery cell [12]. Furthermore, battery components also present an inherent risk to the public, as essential components like the electrolyte mixtures of dangerous compounds.

Common electrolyte mixtures are made up of organic solvents capable of dissolving the electrolyte salt (usually lithium hexafluorophosphate - $LiPF_6$), which permits ion transfer between electrodes

---

* Corresponding authors.
E-mail addresses: Natalia.LEBEDEVA@ec.europa.eu (N. Lebedeva), valentina.busini@polimi.it (V. Busini).

https://doi.org/10.1016/j.fluid.2026.114743
Received 23 February 2026; Received in revised form 15 April 2026; Accepted 18 April 2026

without interfering with electrochemical reactions due to their aprotic nature [13]. As previously mentioned, solvents - like dimethyl carbonate (DMC) - are highly volatile, flammable [14], and toxic [13] compounds, which may generate hazardous atmospheres during evaporation when released as a consequence of electrolyte leakage. As a way of example, only 24.7 mL of DMC are needed to reach dangerous concentrations in a 61.5 m^3 room (volume of a garage with a medium size car and a conservative estimated distance of 0.5 m from the ground to the underside of the vehicle) due to its high toxicity [15].

Since visual confirmation of electrolyte leakage can be difficult due to the high volatility of its components, the need for monitoring systems that are able to identify generated vapours during evaporation are necessary. Since there are no readily available off-the-shelf specific and quantitative solutions for vapour detection [16], the design of fit-for-purpose monitoring systems is needed. The first step for designing such a system is to have a deep understanding of the underlying dynamics of vapour generation and dispersion in a quiescent environment, as this would allow identification of the ideal positioning of the sensors within the environment, and to ensure timely detection of the vapours before the formation of hazardous atmospheres.

Electrolyte vapours generated during the evaporation process tend to accumulate around the evaporating source, behaving like heavy gases because of their greater than air density. An extensive analysis on the underlying physics behind the evaporation and dispersion of electrolyte vapours has been performed in previous works [17,18] with the aid of a computational fluid dynamics (CFD) approach. In the same works, the methodology used also in this study has been experimentally validated through evaporations within an enclosed, quiescent environment (*i.e.,* 1 m^3 aluminium box) of common electrolyte solvents.

As an extension of previously developed models, this work aims to analyse the behaviour of vapours generated during the evaporation of the electrolyte in a larger system. The following electrolyte leakage scenario was simulated: the leakage of a battery cell from an electric vehicle resulting in the accumulation of a pool of liquid electrolyte, within an enclosed garage with no ventilation system. The previously developed models were applied for the new environment, showing their adaptability and wide-range applicability for more realistic release scenarios. Two approaches were evaluated to simulate electrolyte leakage: (i) modelling the evaporation of the complete electrolyte solution ($LiPF_6$ in DMC:PC, *i.e.*, dimethyl carbonate and propylene carbonate), and (*ii*) modelling the evaporation of the pure solvent, DMC, alone.

An in-depth analysis of the evolving vapour cloud was performed, highlighting the inherent differences between the evaporation and dispersion of electrolyte vapours within a small-scale and large-scale systems.

2. Materials and methods

2.1. Numerical approach

The tested setup was performed with Fluent from Ansys Workbench 2024R2, and post processed with CFD-Post and Python version 3.12.0. The CFD method works by solving a system of linearised conservation equations of momentum, mass and energy within a computational domain with a finite volume. While many models to solve the equation system exist, the industry standard, Reynolds-Average Navier-Stokes (RANS) model has shown good results when simulating the convection-diffusion dispersion of heavy vapours [17–19].

Although the presented work deals with low velocities flows found during natural convection evaporation, in order to respect mass continuity within the fluid, the mostly radial evolution of the vapour cloud needs to be compensated by the constant entrainment of air above the evaporating pool, leading formation of transitional structures that are difficult to capture with a purely laminar model. This behaviour was clearly demonstrated by Zhang et al. [19], where the simulations of a fluid with low velocities (order of magnitude of 5.2×10^{-2} m/s) were carried out by using the RANS model, with the Shear Stress Transport (SST) closure model. For this reason, this work used the same approach, whilst enabling the Low Reynolds correlations option to ensure simulation stability, as it has shown reliable results when simulating the dispersion of rarefied gases [19–21].

2.1.1. Evaporation model

Due to the complicated interactions between electrolyte components, this work aimed to assess the viability of a simplified approach to the simulation the evaporating electrolyte solution. Hess et al. [14] demonstrated that in common Li-ion battery electrolytes, like a 1 M $LiPF_6$ DMC:PC solution, the presence of PC and the electrolyte salt have little effect on the total vapour pressure on the mixture, as DMC is the only compound that evaporates in any significant amounts.

Within this scenario, an electrolyte leakage from a electric vehicle occurred within an enclosed medium-sized garage with no ventilation system. Assuming a spill of 30 mL of electrolyte, a typical amount of free electrolyte found in factory fresh large-format battery cells [22,23], approximately 15 mL of solvents like DMC and DEC (*ca.* 50% of the solution) would be released. This value was therefore used as the basis for the amount of DMC and DEC considered in this study. Furthermore, results of the simplified electrolyte evaporation simulation containing DMC were compared with results of a full electrolyte solution (0.85 M $LiPF_6$ DMC:PC) evaporation simulation. Overall, the following cases were tested:

- 15 ml pure DMC simulation (simplified approach)
- 15 ml pure DEC simulation (simplified approach)
- 30 ml 0.85 M $LiPF_6$ DMC:PC (1:1 v/v) simulation (full approach)

The maximum radius of the spilled electrolyte must be determined to estimate the evaporation rate for each case. The radius was obtained by first calculating the minimum thickness of the pool, and assuming that this thickness remains constant throughout the evaporation process. To be conservative, it was assumed that no liquid was absorbed by the concrete onto which the leakage occurred. The following equation was used to calculate the pool thickness, depending on thermophysical characteristics of the simulated compounds [24]:

$$h_{pool} = 2\sqrt{\frac{\sigma_i}{\rho_l g}}\sin\frac{\theta_e}{2} \quad (1)$$

Where σ_i is the surface tension of the simulated compound, ρ_l is the liquid density, g is the gravitational acceleration, and θ_e is the contact angle between the liquid and the surface onto which the liquid was spilled.

Estimating the contact angle is challenging because it depends on the interfacial tension between the liquid, the substrate, and the surrounding environment. However, liquids with similar surface tension are expected to exhibit comparable wetting behaviour on the same surface.

Since no literature data is available for the contact angle between battery electrolyte and concrete, this work assumes that a liquid with similar surface tension—specifically diesel—will display a similar contact angle on concrete. Adia-Mora et al. [25] assumed a contact angle of 20° for diesel on concrete. Given that the surface tension of diesel (28.73 mN m^{-1} at 25 °C [26]) is very close to those of common electrolyte solvents (29.85 mN m^{-1} for DMC [26] and 26.3 mN m^{-1} for DEC [27]), the same contact angle was used in Eq. (1). Because DMC and DEC are very similar in their thermophysical properties, Eq. (1) yields nearly identical pool-thickness values of approximately 0.58 mm for both solvents.

A similar approach was used for the electrolyte solution of $LiPF_6$ DMC:PC, with additional considerations: compared to pure DMC, the electrolyte mixture has a higher contact angle due to the presence of PC. Sun et al. [28] demonstrated this through precise measurements of the

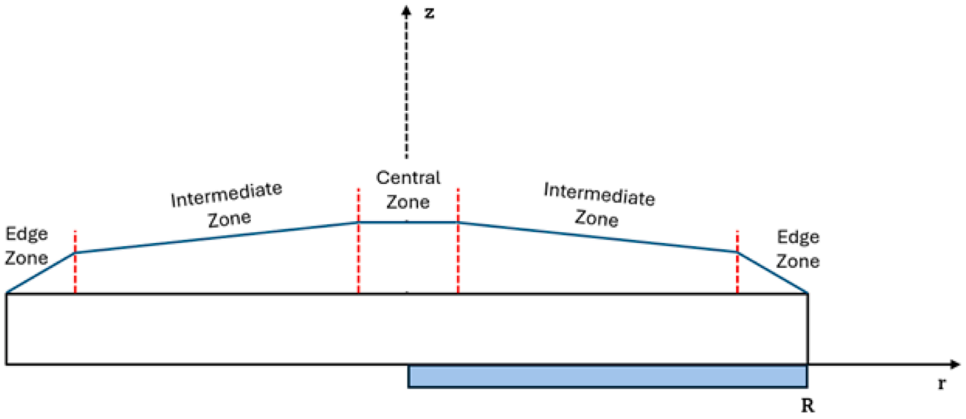

Fig. 1. Scheme of each evaporating source above the evaporating pool.

contact angle of 0.76 M LiPF6 DMC and 0.85 M $LiPF_6$ DMC:PC solutions on polypropylene membranes, where the latter had a contact angle that was about 54.8% higher than the former. As such, the same proportional change was assumed in this paper, *i.e.*, the full electrolyte solution of $LiPF_6$ DMC:PC was assumed to also have a contact angle with concrete which was 54.8% higher than that of pure DMC and concrete. Thus, a 30.96° contact angle was used for the 0.85 M $LiPF_6$ DMC:PC solution simulated. Sun et al. also measured a surface tension of about 35 mN m^{-1}, which was used in Eq. (1) to define a thickness of 0.91 mm for the 0.85 M $LiPF_6$ DMC:PC solution. To calculate the maximum radius, the following equation was used:

$$R_{max} = \sqrt{\frac{V_l}{\pi h_{pool}}} \tag{2}$$

Where V_l is the volume of the studied case. With Eq. (2), the maximum radius for DMC and DEC was estimated to be 9 cm, while 10.2 cm for the 0.85 M LiPF6 DMC:PC solution. Note that as DMC evaporates from the solution, its composition changes, increasing the overall density of the liquid mixture, and decreasing the thickness of the pool (see Solver setup section). This value was used to calculate the initial evaporation rate at the beginning of all cases.

The evaporation model used here is an extension of a previous work, as it was demonstrated that the use of a spatially-dependent model, specifically applied to the CFD approach, can produce good results for predicting the evaporation rate of electrolyte solvents. Based on the work by Dollet et al. [29], the Dollet approach subdivides the evaporating source into three zones: the central, intermediate and edge zone (See Fig. 1).

Due to the small size relative to other zones, the contribution of the central zone was considered to be negligible, as suggested by Dollet et al. Thus, the evaporation rate model simplifies to the following two equations:

$$Q_{intermediate} = 2\pi MwRD_{ab}(C_s - C_\infty)Gr^{1/5} \tag{3}$$

$$Q_{edge} = 2\pi MwRD_{ab}(C_s - C_\infty) \tag{4}$$

Where R is the radius of the pool made by the leakage, D_{ab} is the diffusion coefficient of the evaporating material in air, Mw is the molar weight of the evaporating compound, C_s and C_∞ are the compound concentration at the interface and at bulk, and Gr is the Grashof number, respectively.

During the evaporation of a pure compounds, application of Eq. (3) and (4) is straightforward, as properties that describe evaporation dynamics are wholly dependent on a single species. On the other hand, when multiple compounds are present in the liquid phase of the evaporating pool, convective/diffusive and partial pressure generated by each species should also be accounted for. A generalised approach to consider multiple component contribution is by adding the evaporation rate of each component with a linear dependency on the concentration differences between the interface and bulk. In the multicomponent system considered in this work, however, only DMC evaporates in significant amounts. Therefore, the following thermodynamic assumptions were adopted:

- Ideal liquid and vapour phases
- Local phase equilibrium at the interface between liquid and vapour phases
- Pseudo mono-component evaporation governed by DMC

The latter assumption is justified by the negligible volatility of the other components. PC has a very low vapour pressure (around 3 Pa at 25 °C [14]) and has been shown to evaporate in negligible amounts under natural convection conditions, as demonstrated by the evaporation tests by Seo et al. [30], while LiPF6 remains in the solid phase at room temperature. Consequently, from a thermodynamic perspective, their contribution to the vapour phase can be neglected.

The vapour phase is treated as an ideal gas mixture, which is reasonable given the low pressures and dilute concentrations involved. As such, compound concentration in the vapour phase are calculated as follows:

$$C_i = \frac{P_y}{R_u T}; y = s, \infty \tag{5}$$

$$P_{s,i} = P_{ev,i} x_{i,l} \gamma_{i,l} \tag{6}$$

Where R_u is the ideal gas coefficient of 8.314 J/mol K. $P_{ev,i}$, $x_{i,l}$ and $\gamma_{i,l}$ are the partial pressure correlated to the liquid phase, the liquid mole fraction and activity coefficient of *i-species*. For pure substances, Eq. (6) reduces to the vapour pressure of the compound at a given temperature, as there is no interaction with other compounds in the liquid phase, signifying a unitary concentration and activity coefficient.

The total vapour pressure at saturation conditions of a mixture is defined by the sum of the saturation partial vapour pressure of each component of the liquid mixture [31]. Nevertheless, due to the low volatility of PC and that $LiPF_6$ being a solid, their overall contribution to the total pressure is minimal, such that they may be neglected. By assuming a unitary activity coefficient, the only property that changes as the evaporation occurs is the concentration of DMC within the liquid pool, which reduces in time. Hess et al. [14] demonstrated that using a unitary activity coefficient to account for intermolecular interactions in the liquid phase of an electrolyte mixture was viable to estimate their flash point temperature when compared to experimental data.

Another important parameter included in Eq. (3) is the Grashof number, defined as:

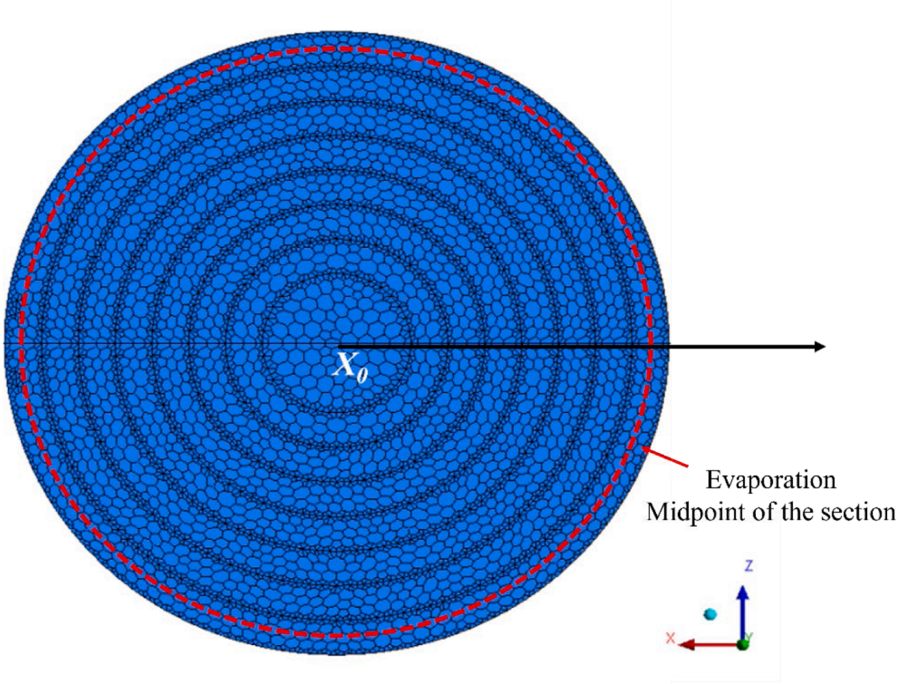

Fig. 2. Mesh of the evaporating source of the evaporating pool.

$$G_r = \left(\frac{\rho_s - \rho_\infty}{\rho_\infty}\right)\frac{{R_h}^3 g}{\nu^2} \tag{7}$$

Where the R_h is the hydraulic radius (*i.e.,* the ratio between the surface area and perimeter) of the evaporating source, ρ_s and ρ_∞ are the vapour densities at the interface and bulk, respectively. ν is the kinematic viscosity of air, which is set at 1.541×10^{-5} m^2/s at 21 °C [31]. Bulk quantities used to estimate the convection-based contribution of the model are defined by measuring simulated values by the CFD model at a chosen distance. This approach allows for the coupling of the evaporation model and the dispersion model; they dynamically affect each other during the simulation. The bulk distance was defined by using the characteristic length of the evaporating source, as done in previous works [17,18], *i.e.*, the maximum radius of the electrolyte pool.

The contribution of each equation is measured depending on the position of the cell within the computational domain. As such, distance from the centre of the evaporating pool of each cell must be considered to define the contribution of each individual cell. Since the origin of the frame of reference (X_0) of the domain is the same as the centre of the evaporating pool, as shown in Fig. 2, the following equation can be used:

$$r = \sqrt{x^2 + z^2} \tag{8}$$

Where x and z are the coordinates of the cell in the ZX plane. Starting from X_0, a transition from the Eqs. (3) and (4), at the edge of the evaporating source, is used to estimate the overall evaporation rate of the pool. To avoid any computational instabilities that could come from using a stepwise function [32], a smoothing function between the two equations was used to ease the transition from one equation to the other:

$$\sigma_t = \frac{1}{1 + exp^{\left(\frac{-(r-n_t)}{m_t}\right)}} \tag{9}$$

Where the smoothing parameters n and m are the centre of transition and transition width, respectively. In previous work [17], implementation of this approach was straightforward, as the evaporation rate was estimated by considering an evaporating source with a fixed radius, since the liquid was contained in a Petri dish. The leakage scenario presented in this work instead attempts to replicate the effect of the realistic release of liquid electrolyte from a battery cell, with the pool of liquid then accumulating underneath the vehicle. As such, not only is the evaporation rate affected by changes of temperature and concentration around the pool, but also by a constant radius decrease as liquid evaporates.

To account for this effect, the evaporation rate within this model dynamically decreases as time changes at fixed intervals. In fact, the evaporating source is divided into different sections with decreasing

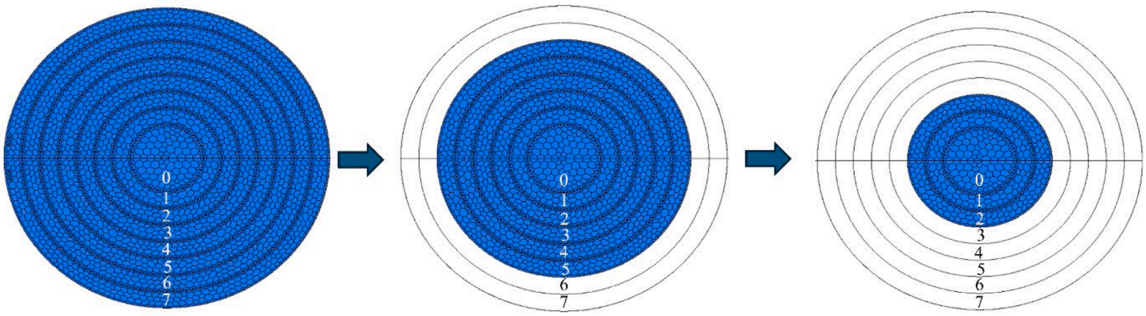

Fig. 3. Radius reduction of the pool, with each section numerated from 0 to 7. Sections “switch off” as simulated time advances due to evaporation.

Table 1
Tabulated n and m values for each Q_t section for the evaporation of pure compound.

t	Radius [m]	Area [m^2]	Evaporation midpoint [m]	Percentage of total mass [%]	n_t	m_t
0	0.02	0.0012	0.01	5.01	0.0112	0.0012
1	0.03	0.0028	0.015	11.2	0.0168	0.0028
2	0.04	0.005	0.02	19.86	0.0224	0.0049
3	0.05	0.0078	0.025	30.97	0.028	0.0078
4	0.06	0.0113	0.03	44.54	0.0336	0.0112
5	0.07	0.0154	0.035	60.97	0.0392	0.0153
6	0.08	0.0202	0.04	79.05	0.0448	0.0201
7	0.09	0.0255	0.045	100	0.0504	0.0253

Table 2
Tabulated n and m values for each Q_t section for the evaporation of electrolyte solution.

t	Radius [m]	Area [m^2]	Evaporation midpoint [m]	n_t	m_t
0	0.075	0.018	0.0375	0.042	0.018
1	0.082	0.0211	0.041	0.0459	0.021
2	0.087	0.0238	0.0435	0.0487	0.0237
3	0.092	0.0266	0.046	0.0515	0.0265
4	0.097	0.0296	0.0485	0.0543	0.0294
5	0.102	0.0327	0.051	0.0571	0.0325

radii, with a 1 cm difference between each one (see Fig. 2). By using the initial evaporation rate of each section, it is possible to estimate the time necessary for the evaporating source to lose a certain amount of material, and thus, a certain radius size.

Once the estimated evaporation time has been simulated, the outer section of the evaporating source is turned into a wall boundary condition, removing its contribution and reducing the total evaporation rate, as shown in Fig. 3. Therefore, each section was defined by using unique centre and width of transition parameters (see Eq. (9)), dependent on the geometrical differences between the geometry from previous work (*i.e.,* the Petri dish) and this work:

$$n_t = \frac{n_{petri\ dish}}{x_{c,pd}} x_{c,t} \tag{10}$$

$$m_t = \frac{m_{petri\ dish}}{A_{pd}} A_{pool,t} \tag{11}$$

Where $n_{petri\ dish} = 0.028$ and $m_{petri\ dish} = 0.00782$ are the centre of transition and transition width from the Petri dish. These parameters have been defined through a linear regression fitting between simulated and experimental evaporation results. More details on how these have been obtained can be found elsewhere [17]. Values $x_{c,pd} = 0.025$ m and A_{pd}=0.00785 m^2 are the evaporation midpoint of the section (see Fig. 2) and total area of the Petri dish, respectively. Likewise, $x_{c,t}$ and $A_{pool,t}$ are the centre and total area of the pool of a given section.

Through the definition of the area and centre of the pool, Eqs. (10) and (11) were used to calculate the centre of transition (n) and width of transition (m) of each section. Results on how these values change depending on the section t are indicated in Table 1 for DMC and DEC, while values for the electrolyte solution are presented in Table 2, where a different surface area was considered due to the different maximum radius estimated. Variations of the electrolyte solution were considered until DMC had fully evaporated.

The evaporation rate of section 0, the one with the smallest radius, was calculated as:

$$Q_0 = Q_{intermediate,0}(1 - \sigma_0) + Q_{edge,0}\sigma_0 \tag{12}$$

All other sections, instead use the following equation:

$$Q_t = Q_{intermediate,t}(1 - \sigma_t) + Q_{edge,t}\sigma_t - \sum_{t=1}^{k} Q_{t-1} \tag{13}$$

And the overall evaporation rate:

$$Q_{tot} = \sum_{t=0}^{k} Q_t \tag{14}$$

Where k is the total number of sections. An example of the decrease of the evaporating source is shown in Fig. 3. Common practice dictates that once 95% of the initial mass of the spilled liquid has evaporated, the pool can be considered as fully evaporated [33]. As such, once the radius of the pool with only 5% of the initial mass has been reached, all inlet boundary conditions were disabled, stopping the evaporation process, whilst letting the dispersion continue. This occurs when the pool reaches a radius of 2 cm, as shown in Table 1.

2.1.2. *Temperature model*

To fully account for evaporation rate changes as the simulation progresses, the temperature change is accounted for by using a local heat balance of the liquid phase. This approach has proven to produce good results in previous work [17], by using the following equation:

$$m_l C_{p,l} \frac{\partial T}{\partial t} = -Q_{tot}\Delta H_{ev} + q_{conv} + q_{cond} \tag{15}$$

Where $C_{p,l}$ is the heat capacity of the liquid phase, ΔH_{ev} is the heat of evaporation, and q_{conv} and q_{cond} are the convective and conductive fluxes from the heat exchange with the environment and the injection ground, respectively. m_l is the weight of the liquid, which changes with the surface area indicated in the previous section. The convective contribution is defined as:

$$q_{conv} = \frac{A}{R_H} \lambda_{air} Nu (T_\infty - T) \tag{16}$$

Where T_∞ and T are the bulk temperature and temperature of the liquid phase, respectively. A is the surface area of the pool, $\lambda_{air} = 2.55 \times 10^{-2}$ W/m K is the thermal conductivity of air at 21 °C [31]. The conductive contribution, that accounts for the heat exchanged with the ground, was defined by the following equation, which is based on heat penetration theory [33]:

$$q_{cond} = \frac{A\lambda_{concrete}}{\sqrt{\alpha_{concrete}\pi t}} \left(T_{ground} - T\right) \tag{17}$$

Where t is time, $\alpha_{concrete} = 5.9 \times 10^{-7}$ m^2/s is the thermal diffusivity coefficient of concrete, by using heavy concrete properties [33]. $\lambda_{concrete} = 1.3$ W/m K is the thermal conductivity coefficient of heavy concrete [33], and T_{ground} is the temperature of the ground of the garage. For Eq. (16), the Nusselt number (Nu) was used to calculate the heat transfer coefficient that governs the heat exchange of the system. The dimensionless number is defined by the following equation:

$$Ra = \frac{|T - T_\infty| \beta g {R_h}^3}{\alpha \nu} \tag{18}$$

$$Nu = 0.59 Ra^{1/4} \tag{19}$$

Where Ra is the Rayleigh number, R_h is the hydraulic radius, β is the thermal expansion coefficient, which is defined as $1/T_\infty$ for ideal gases, and α is the thermal diffusion coefficient of air (2.10 × 10^{-5} m^2/s at 21 °C [31]). Eq. (19) was designed by Goldstein et al. [34] to estimate the heat exchange during a free convection heat exchange above a horizontal flat surface in a quiescent environment.

2.1.3. *Liquid-vapour interface model*

In a previous work, to define the concentration of the inlet flow of evaporated compound within the domain, an equation that models the dissipation of compound within the material boundary layer above the

Table 3
Parameters of the domain.

	Car	Garage
Length [m]	4.6	6.6
Width [m]	1.7	3.7
Height [m]	1.35	2.35

liquid-vapour interface was used, giving good results [18]. The advantage of this approach is the possibility of simulating the evaporation process without having to simulate the liquid phase, thus avoiding heavy multiphase simulations. As such, the following equations were used to define the molar fraction of the compound in the inlet flow:

$$\delta_m = R/Gr^{1/5} \tag{20}$$

$$x_\delta = 1 - \left(1 - \frac{P_{s,i}}{P_{atm}}\right) exp^{\frac{Q_{tot} R_u T \delta_m}{A D_{a,b} P_{atm} Mw}} \tag{21}$$

Where δ_m is the thickness of the material boundary layer above the vapour-liquid interface, as defined by Dollet et al. [29], A is the surface area of the pool, and x_δ is the mole fraction of the vapour of the evaporated liquid at a distance of δ_m from the interface, which is the edge of the boundary layer. R is the radius of the pool, Gr is the Grashof number expressed in Eq. (7), and $P_{s,i}$ is the partial pressure at saturation conditions described in Eq. (6). Other parameters are the same as the ones described for Eqs. (3) and (4). Thus, Eq. (21) was used to define the molar concentration of the inlet flowrate simulated within this work.

2.2. *Domain geometry and mesh*

The chosen geometry for this work was based on the work of Lebedeva *et al.* [15], by assuming that the garage would have a clearance of 1 m from each side of the car, which is of generic design; while clearance underneath the car was set to 21 cm, to simulate a realistic scenario. With these specifications, the size of the car and garage are stated in Table 3. The total volume of the garage is 57.38 m^3.

Mesh and timestep independence were assessed by monitoring variations in DMC concentration (ppm), following the approach previously published work [19,20,35]. Results are shown in Fig. 4. Values were measured above the evaporating pool, at the bulk distance.

With a cell size of 4.25 mm on surface of the ground boundary, the growth rate of 1.05 ensured that the cell size of the domain would slowly increase as distance from the source increased, until it reached the nominal cell size of 5 cm. Due to the difference in the maximum radius of the pool between pure and mixture simulations, two inlet cell sizes were used, which produced meshes with a similar amount of cells. By excluding the volume of the car, the total simulated volume was of 50.7 m^3, with a total of 148 million tetrahedral cells, as it gave acceptable results when compared to finer meshes (see Fig. 4A). By using the symmetry plane approach, the domain was halved, reducing the total number of cells to 74 million cells. Due to stability reasons, the mesh was subsequentially turned into a polyhedral mesh, which further reduced the total cell number to 15.5 million polyhedral cells, with parameters defined in Table 4. To ensure timestep independence, the 15.5 million polyhedral cells was used to ensure simulations stability with a 1 s timestep, as larger values could not reach convergence criteria, resulting in unexpected variations that drastically varied from results obtained with simulations with lower timesteps, as shown in Fig. 4B The first simulated 20 s of each scenario were performed with a timestep of 0.05 s to meet convergence criteria and ensure simulation stability.

To ensure a good concentration gradient close to the source and appropriate interactions with the surface of the simulated care, an inflation layer was applied on both boundary conditions, as shown in Fig. 5. The inflation layer on the inlet has a total thickness of 1 cm and was divided by 18 layers, while the inflation layer on the boundary condition of the car has a total thickness of 5 mm and was divided by 5 layers.

2.3. *Solver setup*

An important step of this simulation is the reduction of the size of the evaporating source. Timed relative to the evaporation rate of the source, the reduction of the area of the source was set at specific times, depending on the volume needed to evaporate.

As a way of example, changes of the evaporation rate of DMC were reported in Table 5. By assuming that the height of the evaporating pool remains a constant of 0.58 mm while the properties of the liquid remain unchanged, the volume difference between a cylinder with a 9 cm radius and an 8 cm radius equals 3.13 ml. With an initial evaporation rate of 4.81 mg/s for DMC, the stated volume evaporates in about 696 s, at which point the surface with the evaporation rate Q_7 was turned into a wall boundary condition. A journal file was setup to transform inlet boundary conditions, defined as Q_t, into wall boundary conditions,

Table 4
Meshing parameters.

	Size [m]	Growth rate [-]	Behaviour
Nominal cell size	0.05	-	-
Inlet pool	0.0036 (for pure compounds)	-	Hard
	0.0033 (for electrolyte mixture)	-	Hard
Car surface	0.005	1.2	Soft
Ground	0.00425	1.05	Soft

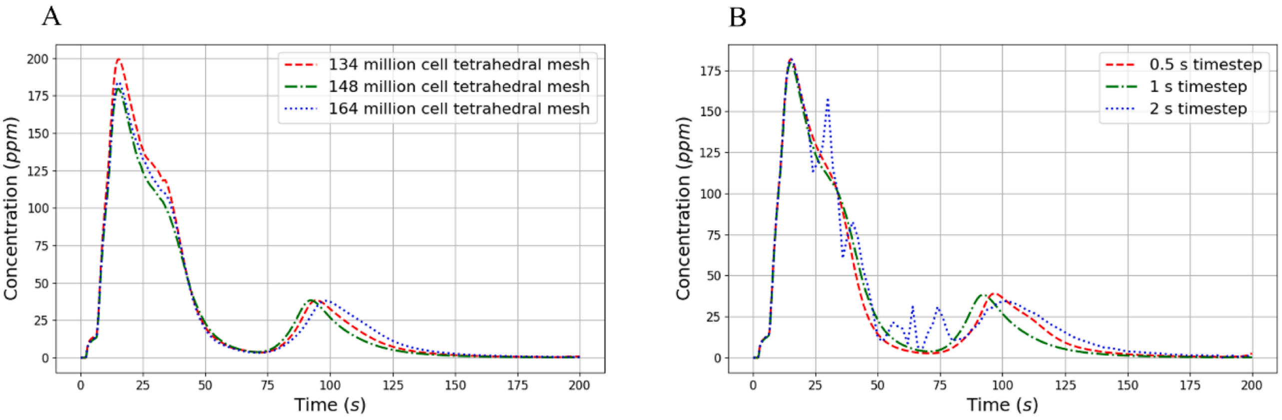

Fig. 4. Mesh (A) and timestep (B) independence with varying mesh sizes and timesteps.

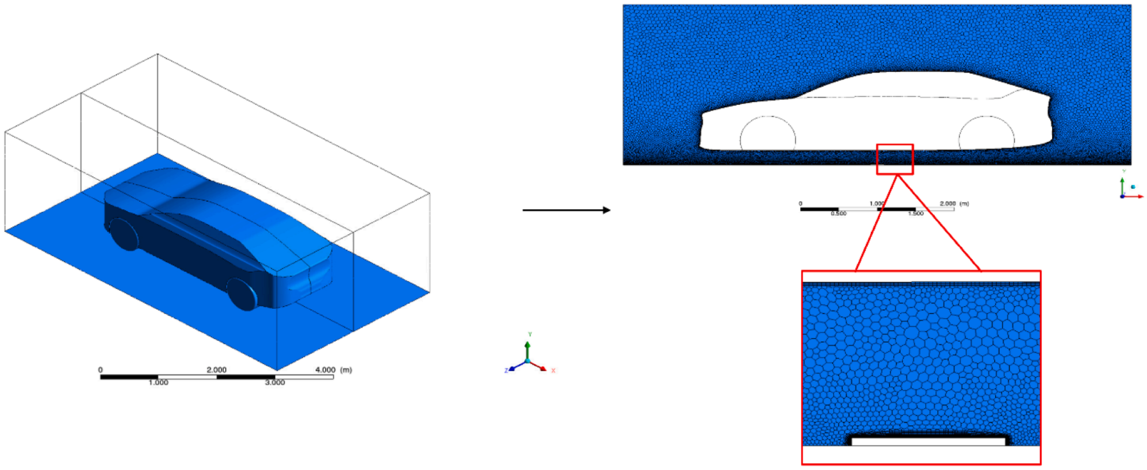

Isometric view of the Geometry

Front view of the mesh

Fig. 5. Geometry and mesh of the garage.

Table 5
Tabulated time at which inlet boundary conditions (Q_t) are removed for pure DMC evaporation.

Q_t	Radius difference	Total volume difference [ml]	Evaporation rate of DMC [mg/s]	Volumetric rate [ml/s]	Time to evaporate [s]
7	0.09–0.08	3.13	4.81	0.0045	696
6	0.08–0.07	2.76	3.73	0.0034	793
5	0.07–0.06	2.40	2.45	0.0023	1045
4	0.06–0.05	2.03	1.98	0.0018	1094
3	0.05–0.04	1.66	1.54	0.0014	1143
2	0.04–0.03	1.29	0.86	0.0008	1597
1	0.03–0.02	0.92	0.76	0.0007	1305

effectively removing their contribution from the evaporation rate. At the same time, the surface area values used in the liquid-vapour interface and temperature models were dynamically updated as well. Inlet boundary conditions were thus removed on the times specified in Table 5. Once the volume relative to 2 cm radius is reached (*i.e.,* 95% evaporated), the pool was considered as fully evaporated, thus turning all inlet boundary conditions to wall boundary conditions. This occurs at 7675 s. Note that the evaporation rate does not remain constant between the stated intervals on Table 5, as it changes depending on temperature variations of the pool and vapour accumulation around the source. The initialisation evaporation rate for each section was used to have a first estimate of the time needed for each volume portion to evaporate. This same method was applied to DEC and $LiPF_6$ in DMC:PC mixture simulations.

An important detail, which highlights the biggest differences between the pure DMC simulation and the electrolyte solution simulation, is the changing concentration of DMC within the liquid phase. Table 7 shows how the volumetric reduction of the pool due to evaporation leads not only to a change of radius, but also a decrease of DMC concentration (with an increase of PC and $LiPF_6$ concentrations as a consequence), pool thickness, and an increase liquid density. Changes to the evaporation rate derived from these changes were accounted for during the evaporation by considering the changing concentration of DMC in Eqs. (6) and (21).

The garage ground and walls, along with the surface of the car were defined through wall boundary conditions, with a no-slip condition and a roughness height value of 0.005 m for smooth concrete [33], and 1×10^{-6} m for the surface of the car [43]. Since the case scenario represents the leakage and evaporation of an electrolyte solution in an enclosed garage with no ventilation, no outlet was defined.

Concentration of the DMC were sampled at different points within the domain to assess the dispersion speed at critical distances from the centre of the domain. Position of these points are listed in Table 8 and shown in Fig. 6. An additional point is measured at 15 cm directly above the base, defined as C in Fig. 6.

Species transport was enabled with multicomponent diffusion and inlet diffusion. The gaseous phase of the solvent was defined through the incompressible ideal gas density model, and by using the vapour properties and compound interactions listed in Table 6. Since the simulation of the full electrolyte solution is performed by considering a negligeable evaporation of PC, only DMC was considered during the simulation. As such, properties of the gaseous phase for the electrolyte simulation were the same as the one used in the pure DMC simulation. Dry air and water

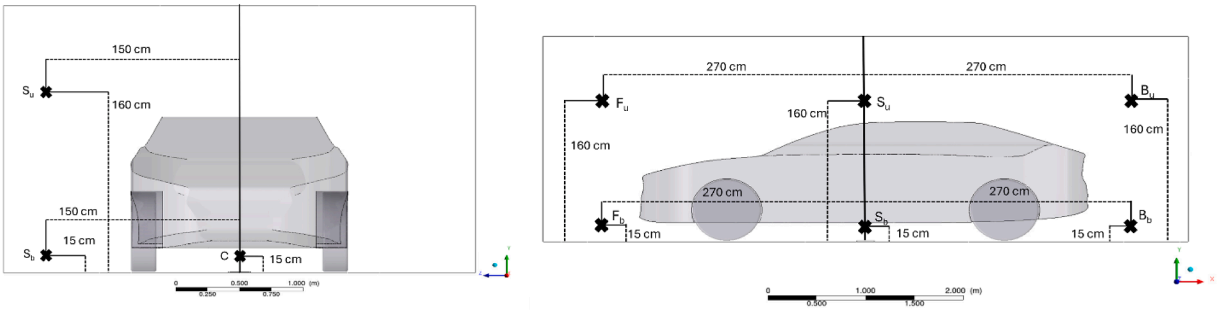

Front view

Side view

Fig. 6. Distances from the centre of the domain of each sampling point considered.

Table 6
Thermophysical characteristics of the DMC and DEC.

Liquid phase thermophysical characteristics	*DMC*	*DEC*
$\boldsymbol{Mw}$ [g/mol]	90.07 [36]	118.13 [37]
ρ [kg / m^3]	1070 [36]	975 [37]
$C_{p,l}$ [J/kg K]	1826.64 [38]	1785.32 [37]
ΔH_{ev} [J/kg]	422,116.13 [39]	378,813.55 [39]
Vapour phase thermophysical characteristics		
$C_{p,v}$ [J/kg K]	1173.94 [40]	989.41 [41]
λ_v [W/m K]	0.01378 [17]	0.0094 [17]
μ_v [Pa s]	9.43 × 10^{-6} [17]	8.46 × 10^{-6} [17]
P_v [Pa]	$10^{6.43-\frac{1413}{T[K]-44.25}}$ x 10^3 [40,42]	$10^{5.883-\frac{1223.77}{T[K]-84.304}}$ x 10^3 [42]
D_{ab} [m^2/s]	6.1 × 10^{-8} x T[K]−8.53 × 10^{-6} [17]	5.108 × 10^{-8} x T[K]−7.178 × 10^{-6} [17]

Table 9
Simulated scenarios of the evaporated compounds.

Compound	Initial room temperature [°C]	Temperature gradient in the box [°C]	Relative Humidity [%]
DMC	21.99	0.26	66%
DEC	22.93	0.45	65%
0.85 LiPF6 DMC:PC	21.99	0.26	66%

Table 10
Protection action criteria values for DMC [44] and DEC [45].

	PAC-1 [ppm]	PAC-2 [ppm]	PAC-3 [ppm]
DMC	11	120	700
DEC	12	130	810

vapour were included to introduce relative humidity values to the environment. Evaporation, temperature and vapour-liquid interface models from Sections 2.1.1, 2.1.2 and 2.1.3 were included in the simulation through a custom-made user-defined function (UDF). Initialisation of the simulation was done by replicating the temperature gradient along the Y-axis of the domain from previous work [18], and using scenario conditions from Table 9.

The RANS simulation was carried out with a pressure-velocity coupled solver, and it used a second upwind scheme to resolve all conservation equations. To guarantee that convergence criteria were met, a timestep of 0.05 s per timestep was required in this case. After the first 20 simulated seconds, the timestep was set to 1 s per timestep. The simulation was run for 8600 s, with an average CPU time of 90 s per timestep. Effects of the surface area change during evaporation on the pure solvent evaporation was explored within the Supplementary Material.

3. Results and discussion

3.1. Dispersion within the domain

As mentioned in Section 1, DMC and DEC are a highly toxic compounds, as defined by the Protection Action Criteria (PAC) listed in Table 10.

PAC values are concentration thresholds for accidental exposures to assess the toxicity risks of compounds, where exposure to concentrations at PAC-2 and PAC-3, can lead to irreversible health and life-threatening effects [44,45]. As such, knowledge of the speed at which hazardous concentrations might be reached at various heights is very useful to design appropriate detection and mitigation measures within the presented case scenario.

Since concentrations at 1.6 m never reached values close to 1 ppm within the simulated time, these are not reported. Similar to the results reported on our previous works [17,18], the vapour generated by the evaporating source spreads radially. Moreover, the farther away from the source, the lower is the concentration of the simulated cloud, and thus, the slower the convection-based dispersion becomes. Since the domain is very large, vertical dispersion due to an obstacle, *i.e.,* the wall, is significantly delayed.

Due to the uneven sizes of the base of the garage, cloud dispersion differs depending on where the measurement is taken. For this reason, it takes at least 1200 s before the 120 ppm isorsurface covers the entire surface for DMC, while no PAC values above PAC 1 were ever reached for DEC, as shown Figs. 7A and 8A. As the S_b point is closer to the wall (see Fig. 6), higher concentrations were reached before all other points where measurements were taken. In fact, by 600 s the isosurface representing the 120 ppm concentration for DMC had already reached the

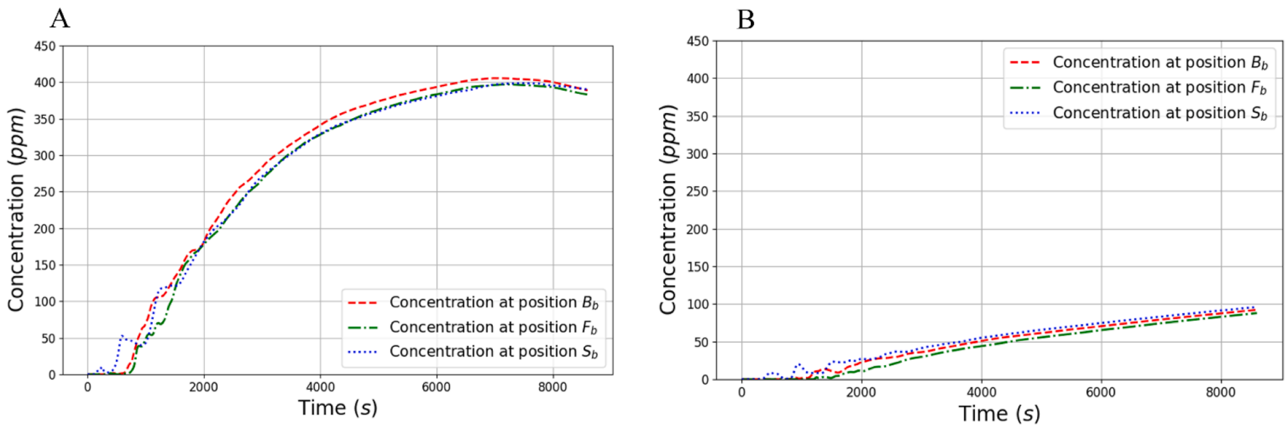

Fig. 7. Dispersion within the domain within the garage at different monitoring points (see Fig. 6) for DMC (A) and DEC (B).

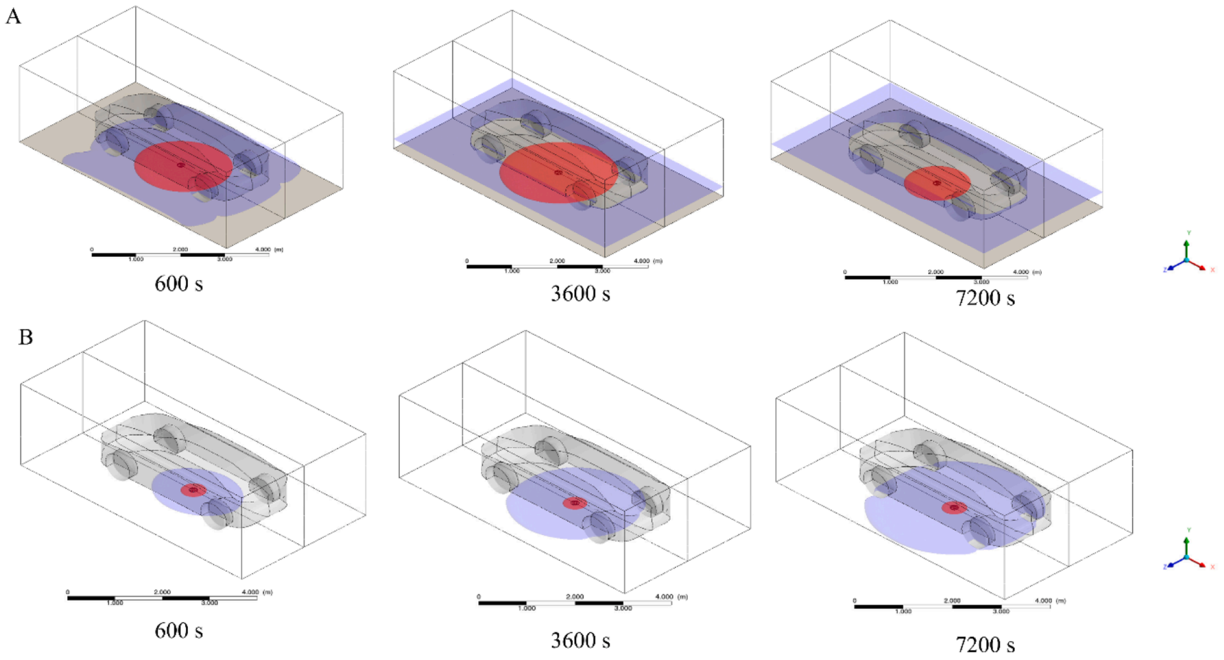

Fig. 8. Vapour cloud evolution of DMC (A) and DEC (B). Blue isosurface = 120 ppm (PAC 2-DMC) and 130 ppm (PAC 2-DEC); red isosurface = 700 ppm (PAC 3-DMC) and 810 ppm (PAC 3-DEC).

wall, and reflected back, spreading to other directions. On the other hand, the 130 ppm concentration never even managed to reach the walls of the garage, as seen in Figs. 7B and 8B

For DMC, the faster spreading vapour, once concentrations close to the walls of the garage have reached high enough values, the cloud homogenises at around 1800 s, at 15 cm.

An interesting aspect to note is the reduction of the vapour cloud isosurface at PAC-3 for DMC shown in Fig. 8A. PAC-3 concentrations never reach the walls of the domain, instead reducing in size after around 3600 s, and fully dissipating around 12 min after the evaporation ended. This may be related to the decreasing evaporation rate as the simulation progresses, as less and less material (*i.e.,* DMC vapour) is

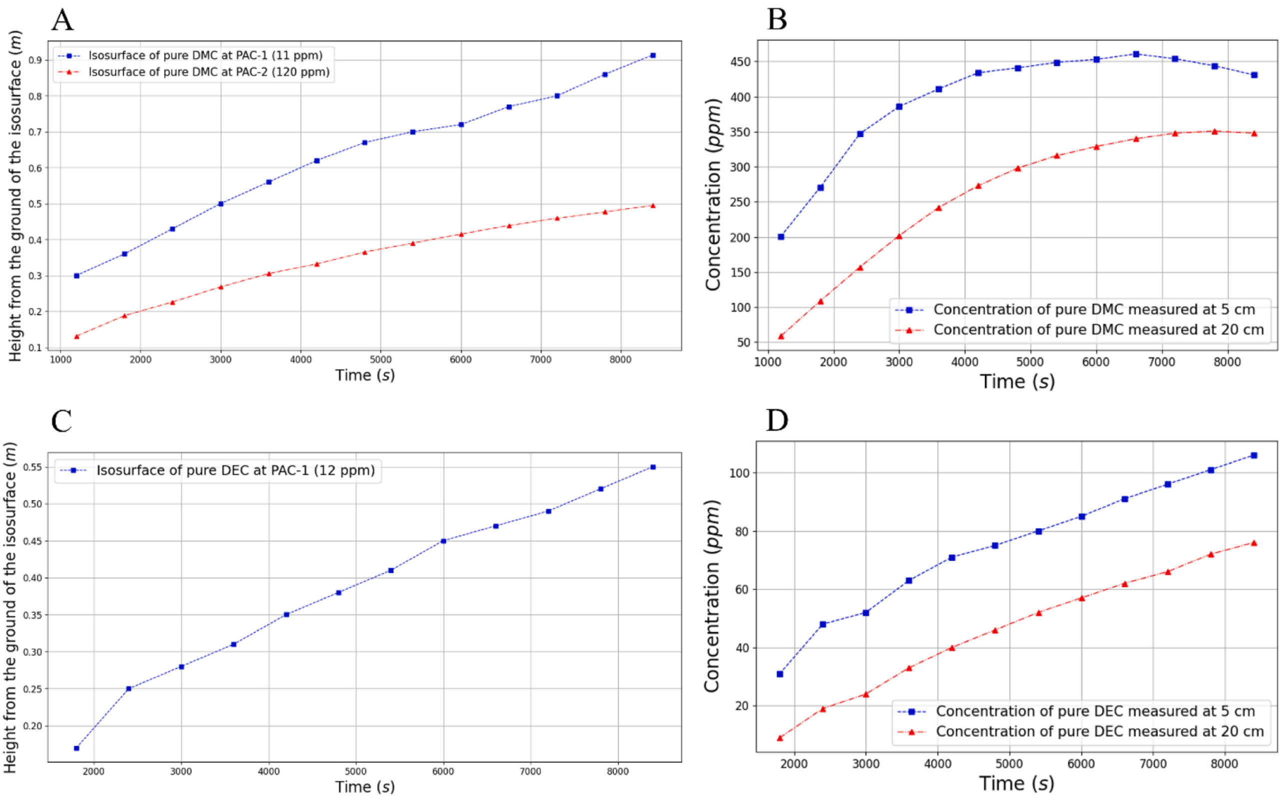

Fig. 9. Height change of the PAC-1 and PAC-2 concentration isosurface and concentrations measured at 5 and 20 cm from the ground for DMC (A and B) and DEC (C and D). Measured at 0.3 m from the back of the car, along the symmetry line.

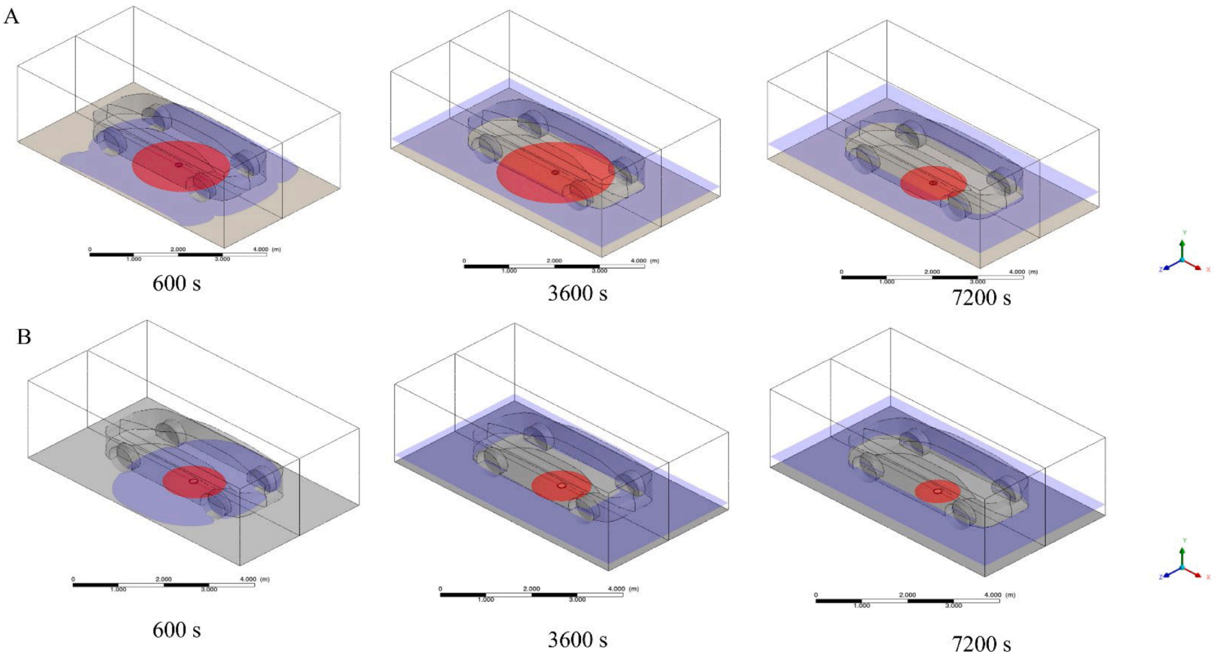

Fig. 10. Vapour cloud evolution of pure DMC (A) and $LiPF_6$ DMC:PC (B). Blue isosurface = 120 ppm (PAC2) red isosurface = 700 ppm (PAC3).

being introduced to compensate for the spread and dissipation of the vapour cloud. Moreover, while the evaporation flux is not enough to compensate for the PAC-3 concentration, it is enough to allow the PAC-2 concentration isosurface to keep growing, as the concentration is almost 6 times smaller.

Conversely, since the DEC influx of material never ceased due to the much slower evaporation rate (at the time DEC simulation stopped, there were still around 9.1 ml of compound remaining), the vapour cloud was shown to only be expanding in Fig. 8B The vapour cloud speed varied at the beginning as it stabilised, to then reach a constant increased rate shown in Figs. 7B and 8B

Independent of the point being measured, concentration growth at 15 cm tended to plateau at around 400 ppm for DMC, while monotonically increasing for DEC.

For DMC, this could be explained by the homogenisation of density at the bottom of the domain, as convection-based dispersion contribution diminishes. As such, as concentration raise, diffusion-based dispersion becomes dominant, which is significantly slower.

For DEC, the monotonous growth comes as a consequence of the lack of density homogenisation at the lower heights of the garage. DMC and DEC would behave similarly due to their thermophysical characteristics, but the lower inlet concentration of DEC (0.21 mol/m^3 for DEC, compared to 1.2 mol/m^3 for DMC) slows the dispersion process significantly, as the dispersion process is mostly convection-based.

Similar to previous work [17,18], it is shown that dispersion speed is dependent on compound properties, although distance from the source and changing evaporation flux demonstrated to have a significant effect as well. Results from Fig. 9 highlight the effect that increasing distance from the source has on the dispersion speed of specific concentration fractions, along with the effect of decreasing evaporation flux on the concentration at fixed points in space. This behaviour was seen for both DMC and DEC:

- Fig. 9A represents the distance traversed vertically by isosurfaces at PAC-1 and PAC-2 concentrations for DMC. For DEC, Fig. 9C shows only the vertical distance travelled by the PAC-1 isosurface, as PAC-2 and PAC-3 never reached the walls of the domain, such that no significant vertical dispersion occurred. While the distance traversed by PAC-2 decreases in time for DMC, PAC-1 has a constant increase of traversed distance for both compounds. The behaviour of the PAC-1 isosurface may be due to its concentration being over 10 times lower than their respective PAC-2. It is then justified to say that the speed of dispersion depends heavily on the concentration of the considered surface; for the DMC scenario, the increasing distance from the source has a slowing effect on dispersion, affecting the heavier fractions first.
- Fig. 9B and D represent the concentration measured at 5 and 20 cm from the ground, where concentration growth rate peaks at 1200 and 2400 simulated seconds for DMC, but never peak for DEC. It is evident that the distance from the source influenced the behaviour of the cloud at the two measured points. This was most evident in the DMC scenario as the plateauing behaviour was visible sooner with the heavier fraction at 5 cm from the source. Whilst not as represented in the DEC scenario, there was a noticeable decrease in the dispersion rate between 2600 and 4200 s for the heavier fraction at 5 cm from the source.

It is evident that the size of the domain is extremely influential on the cloud evolution of pure electrolyte solvents, especially if the evaporation occurs in a quiescent domain, such as the one presented in this work. Furthermore, within a significantly bigger domain, diffusion-based dispersion becomes dominant much quicker, as vapour accumulation takes longer. Combined with a consistent reduction in evaporation flux, *i.e.*, material introduced within the domain, the overall dispersion of DMC and DEC vapour remained limited, where PAC-2 concentrations barely reached a height of 50 cm from the ground for the former, while never going over 10 cm for the latter.

3.2. *Comparison between pure DMC simulation and electrolyte mixture*

In this section the advantages and disadvantages of simulating the electrolyte mixture as a pure component are highlighted. As such, only the results from the pure DMC simulation were compared with the full electrolyte scenario.

The first immediate difference highlighted in Fig. 10 is the dimension of the DMC vapour cloud that was generated during the evaporation. Similar to pure DEC, vapours released from the electrolyte solution spread slower than the ones generated by the evaporation of pure DMC.

Table 7
Properties of the electrolyte mixture during the evaporation.

	Total volume [ml]	Mixture density [g/cm^3]	Pool thickness [mm]	Radius [m]	Volume of DMC [ml]	Mole fraction of X_{DMC}	Mole fraction of X_{PC}
0	30	1.212	0.92	0.102	14.31	0.467	0.472
1	26.98	1.228	0.91	0.097	11.3	0.406	0.512
2	24.08	1.247	0.9	0.092	8.4	0.34	0.573
3	21.33	1.270	0.89	0.087	5.65	0.257	0.645
4	18.78	1.297	0.88	0.082	3.1	0.159	0.729
5	15.78	1.342	0.87	0.075	0	0	0.864

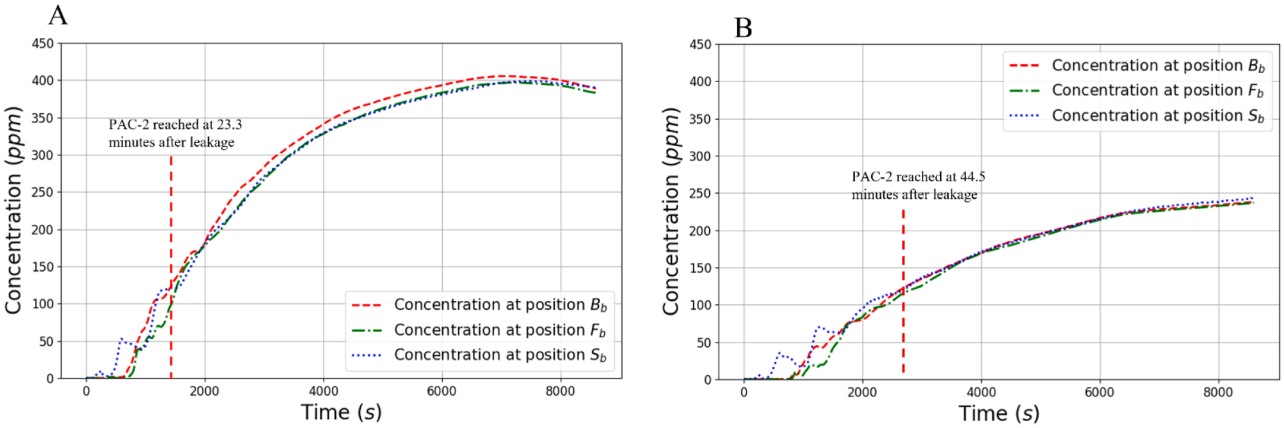

Fig. 11. Dispersion within the domain within the garage at different monitoring points for pure DMC (A) and the full electrolyte solution of LiPF$_6$ DMC:PC (B). PAC-2 was reach at 1400 s and 2670 s for the pure DMC and full electrolyte solution scenario, respectively.

Table 8
Coordinate of sampling points within the domain.

	X [m]	Z [m]
Bottom (positioned at 15 cm from the ground)		
Front (F_b)	−2.7	0
Back (B_b)	2.7	0
Side (S_b)	0	1.5
Upper (positioned at 1.6 m from the ground)		
Front (F_u)	−2.7	0
Back (B_u)	2.7	0
Side (S_u)	0	1.5

The reason for this behaviour is two-fold:

- With an evaporation flux that is only 37.5% that of the pure DMC scenario, the full electrolyte solution evaporation flux was severely limited by the surface area change and the concentration reduction of DMC within the liquid phase (see Eq. (3), (4) and (7)), which was over 50%, as shown in Table 7.
- A lower percentage of the solvent in the solution leads to a lower vapour concentration of the simulated compound within vapour phase, thus limiting the driving force of the convection-based dispersion mechanism. With an initial vapour concentration of 0.55 mol/m^3, this only corresponded to 45.8% of the initial vapour concentration of the pure DMC scenario.

During the evaporation, the concentration of DMC in the liquid phase solution kept decreasing as it evaporated, lowering to 0.42 mol/m^3 and 0.32 mol/m^3 at 3450 s and 5890 s after the electrolyte leakage, respectively.

For this reason, there is an evident decrease in the size of the heavier fraction of the vapour cloud for the full electrolyte solution scenario that

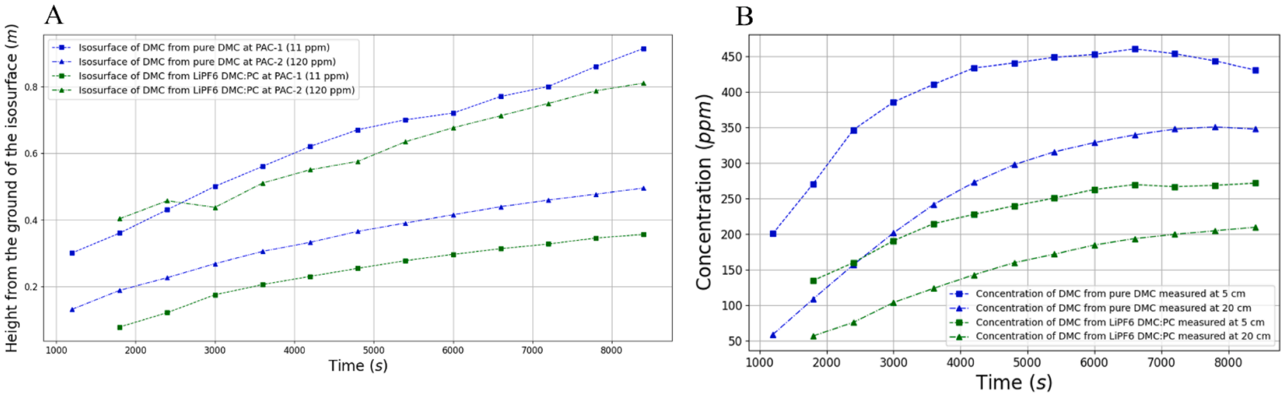

Fig. 12. Comparison between DMC and LiPF$_6$ DMC:PC vapours of height change of the PAC-1 and PAC-2 concentration isosurface (A) and concentrations measured at 5 and 20 cm from the ground (B) for DMC (A). Measured at 0.3 m from the back of the car, along the symmetry line.

began at around 3600 s, as shown in Fig. 10. While in the pure DMC scenario the vapour concentration of DMC remained constant throughout the simulated period, the decreasing concentration of DMC for the full electrolyte solution scenario in the liquid phase had an evident effect on the dispersion speeds of the cloud.

The slower dispersion would, therefore, lead to different predictions, *i.e.,* the time of dispersion for specific vapour fractions within the computational domain. Fig. 11 compares dispersion results at the sampling points indicated in Table 8, at the lower sections of the domain, where a similar behaviour between scenarios can be seen. Like the pure DMC scenario, the vapour cloud in the full electrolyte scenario (see Fig. 11B) grew monotonously for most of the simulated time, seemingly reaching its peak at around 8500 s after the electrolyte leakage, with 241 ppm.

Dispersion predictions performed within the pure DMC scenario show that the PAC-2 (120 ppm) level was reached by all studied measurement points at around 1400 s, while the slower dispersion of the full electrolyte scenario shows that the PAC-2 level was reached at around 2670 s, taking almost twice as much time.

Results from Fig. 12A show that:

- The average dispersion speed for DMC vapours with a concentration of PAC-1 have a 23.3 % reduction when using the full electrolyte model instead of the pure DMC model
- The average dispersion speed for DMC vapours with a concentration of PAC-2 have a 27.7 % reduction when using the full electrolyte model instead of the pure DMC model

Furthermore, Fig. 12B shows how the overall slowing of the vapour cloud affects the peak concentration reachable by the scenario with the full electrolyte solution. Peak values at 5 cm from the ground were reached around 1500 s slower, at 350 ppm as it plateaus. It is important to note that the general behaviour of the cloud remains the same, as the geometry was not changed between scenarios.

As such, results from Fig. 11 and 12 demonstrate that a simplifying model like the pure DMC scenario would not be able to replicate results expected from the full electrolyte scenario, as the dependence of the carbonate solvent concentration in the liquid phase has a strong effect on the dispersion. Even though it is a more complex task to develop and implement a full electrolyte model, the electrolyte leakage incidental scenario cannot be simplified to a single component scenario.

4. Conclusion

An evaporation and dispersion dynamics study of electrolyte was carried out in this work. The presented CFD model (*i.e.*, evaporation model and dispersion model) was previously designed and tested in a 1 m^3 aluminium box, demonstrating its ability to predict the dispersion rate of DMC and DEC in an enclosed, quiescent environment. The model was successfully used in a larger and more complex environment. Moreover, to further explore the consequences of an electrolyte leakage from an electric vehicle, not only the release of pure solvents but also the full electrolyte solution of $LiPF_6$ DMC:PC within a garage with no ventilation system was used for this work. By considering the worst case scenario, all three scenarios were simulated, and a thorough study of the evolution of the vapour cloud was performed.

Multiple aspects may be highlighted regarding the evaporation and dispersion models utilised:

- Due to a significantly larger system of the garage (50.7 m^3) obstacle-induced vertical dispersion was found to be limited.
- Since heavier-than-air vapours spread radially, accumulation of vapours around the evaporating source is hampered, thus having little effect on evaporation flux, which in turn, is mostly dependent on the area reduction of the pool during the evaporation.
- Temperature changes of the pool due to the evaporation of DMC, DEC and DMC within the $LiPF_6$ DMC:PC solution were fully compensated by the conductive heat transfer by the ground. Thus, the temperature of the electrolyte pool remains almost constant, as expected for non-boiling liquids [33].

Dangerous concentrations indicated by PAC values remain relatively close to the ground, with PAC-1 concentrations never going over the 1 m height from the ground and PAC-2 reaching only 50 cm from the ground for both compounds in the studied system and within the simulated time considered.

It is evident that heavier fractions of the cloud are more significantly affected by increased distance from the source, as dispersion speed decrease with distance, and by lower evaporation rates as the surface area of the source decreases.

The most dangerous vapour concentrations related to the evaporation of electrolyte after an electrolyte leakage incident are close to the ground, because of the radial dispersion of heavy vapours generated. As such, when designing an efficient monitoring and detection system, sensor positioning must be at ground level.

Lastly, throughout this work, a simplified electrolyte evaporation model of a single solvent (DMC) was used and compared with a model that accounts for the full electrolyte solution ($LiPF_6$ DMC:PC). It was shown that this simplified method of simulating the electrolyte leakage scenario would predict a significantly higher concentration of a component (DMC) in the vapour at a given coordinate and time compared to that in the simulation of a full electrolyte solution. For the system studied in this work, if a detection threshold is set to PAC-2 values, *i.e.,* 120 ppm of DMC, the leakage may be identified within the first 25 min for the pure DMC scenario, while it would take 44.5 min for the leakage to be detected with the full electrolyte solution scenario (with sensors placed at around 15 cm from the ground).

Future work would expand the scope of the evaporation and dispersion model, not only by experimentally validating it, but by also accounting all other interactions the electrolyte solution might have with the surrounding environment, like the generation of dangerous species by having the moisture of air interacting with the electrolyte salt. This would provide a more realistic view of the various interactions that the entire electrolyte mixture may have with the model.

Acknowledgements

This work was realised with the collaboration of the European Commission Joint Research Centre, under the Collaborative Doctoral Partnership Agreement No. 35,455.

CRediT authorship contribution statement

Fabio Ferrario: Writing – original draft, Visualization, Software, Formal analysis, Conceptualization. **Natalia Lebedeva:** Writing – review & editing, Supervision, Funding acquisition, Conceptualization. **Valentina Busini:** Writing – review & editing, Supervision, Software, Funding acquisition, Data curation, Conceptualization.

Declaration of competing interest

The authors declare that they have no known competing financial interests or personal relationships that could have appeared to influence the work reported in this paper.

Supplementary materials

Supplementary material associated with this article can be found, in the online version, at doi:10.1016/j.fluid.2026.114743.

Data availability

Data will be made available on request.

References

[1] K. Abbass, M.Z. Qasim, H. Song, M. Murshed, H. Mahmood, I. Younis, A review of the global climate change impacts, adaptation, and sustainable mitigation measures, Environ. Sci. Pollut. Res. 29 (28) (Jun. 2022) 42539–42559, https://doi.org/10.1007/s11356-022-19718-6.

[2] L. Wang, L. Wang, Y. Li, J. Wang, A century-long analysis of global warming and earth temperature using a random walk with drift approach, Decis. Anal. J. 7 (Jun. 2023) 100237, https://doi.org/10.1016/j.dajour.2023.100237.

[3] “Sea level rise: everything you need to know,” World Economic Forum. Accessed: Jul. 05, 2025. [Online]. Available: https://www.weforum.org/stories/2025/03/rising-sea-levels-global-threat/.

[4] Y. Ghorbani, S.E. Zhang, G.T. Nwaila, J.E. Bourdeau, D.H. Rose, Embracing a diverse approach to a globally inclusive green energy transition: moving beyond decarbonisation and recognising realistic carbon reduction strategies, J. Clean. Prod. 434 (Jan. 2024) 140414, https://doi.org/10.1016/j.jclepro.2023.140414.

[5] Y. Ghorbani, et al., The strategic role of lithium in the green energy transition: towards an OPEC-style framework for green energy-mineral exporting countries (GEMEC), Resour. Policy 90 (Mar. 2024) 104737, https://doi.org/10.1016/j.resourpol.2024.104737.

[6] P. Parvizi, M. Jalilian, A.M. Amidi, M.R. Zangeneh, J.-R. Riba, From present innovations to future potential: the promising journey of lithium-ion batteries, Micromachines (Basel) 16 (2) (Feb. 2025) 194, https://doi.org/10.3390/mi16020194.

[7] Q. Zhang, Y. Shang, Y. Li, R. Zhu, A concise review of power batteries and battery management systems for electric and hybrid vehicles, Energies 18 (14) (Jul. 2025) 3750, https://doi.org/10.3390/en18143750.

[8] “Lithium-ion batteries: a growing fire risk,” British Safety Council. Accessed: Jul. 02, 2025. [Online]. Available: https://www.britsafe.org/safety-management/2024/lithium-ion-batteries-a-growing-fire-risk.

[9] D. Lu and D.L.S. writer, “‘Fastest-growing fire risk’: why do lithium batteries keep exploding across Australia?,” *The Guardian*, Nov. 14, 2024. Accessed: Jul. 02, 2025. [Online]. Available: https://www.theguardian.com/technology/2024/nov/15/lithium-ion-battery-explosions-why-fire-risk-e-bikes.

[10] Z. An, T. Shi, X. Du, X. An, D. Zhang, J. Bai, Experimental study on the internal short circuit and failure mechanism of lithium-ion batteries under mechanical abuse conditions, J. Energy Storage 89 (Jun. 2024) 111819, https://doi.org/10.1016/j.est.2024.111819.

[11] C. Essl, A.W. Golubkov, A. Fuchs, Influence of aging on the failing behavior of automotive lithium-ion batteries, Batteries 7 (2) (Apr. 2021) 23, https://doi.org/10.3390/batteries7020023.

[12] Y. Wang, C. Zhang, J. Hu, P. Zhang, L. Zhang, L. Lao, Investigation on calendar experiment and failure mechanism of lithium-ion battery electrolyte leakage, J. Energy Storage 54 (Oct. 2022) 105286, https://doi.org/10.1016/j.est.2022.105286.

[13] K. Xu, Nonaqueous liquid electrolytes for lithium-based rechargeable batteries, Chem. Rev. 104 (10) (Oct. 2004) 4303–4418, https://doi.org/10.1021/cr030203g.

[14] S. Hess, M. Wohlfahrt-Mehrens, M. Wachtler, Flammability of Li-ion battery electrolytes: flash point and self-extinguishing time measurements, J. Electrochem. Soc. 162 (2) (2015) A3084–A3097, https://doi.org/10.1149/2.0121502jes.

[15] N.P. Lebedeva, L. Boon-Brett, Considerations on the chemical toxicity of contemporary Li-ion battery electrolytes and their components, J. Electrochem. Soc. 163 (6) (2016) A821–A830, https://doi.org/10.1149/2.0171606jes.

[16] S. Hildebrand, F. Ferrario, N. Lebedeva, Comparative overview of methods for the detection of airborne electrolyte components released from lithium-ion batteries, Energy Technol 12 (1) (Jan. 2024) 2300647, https://doi.org/10.1002/ente.202300647.

[17] F. Ferrario, S. Hildebrand, R. Da Costa Barata, M. Lazareanu, N. Lebedeva, V. Busini, Li-ion battery electrolyte vaporisation model: an experimental and computational fluid dynamics approach, Energy Rep 14 (Dec. 2025) 4308–4323, https://doi.org/10.1016/j.egyr.2025.11.028.

[18] F. Ferrario, S. Hildebrand, R. da Costa Barata, M. Lazareanu, N. Lebedeva, V. Busini, Simulation of Li-Ion battery electrolyte vapour dispersion in an enclosed and quiescent environment: an experimental and computational fluid dynamics approach, J. Energy Storage 137 (Jan. 2025), https://doi.org/10.1016/j.est.2025.118495.

[19] Y. Zhang, L. Wang, A. Li, P. Tao, Performance evaluation by computational fluid dynamics modelling of the heavy gas dispersion with a low Froude number in a built environment, Indoor Built Environ 29 (5) (Jun. 2020) 656–670, https://doi.org/10.1177/1420326X19856041.

[20] L. Dong, H. Zuo, L. Hu, B. Yang, L. Li, L. Wu, Simulation of heavy gas dispersion in a large indoor space using CFD model, J. Loss Prev. Process Ind. 46 (Mar. 2017) 1–12, https://doi.org/10.1016/j.jlp.2017.01.012.

[21] V. Busini, R. Rota, Influence of the shape of mitigation barriers on heavy gas dispersion, J. Loss Prev. Process Ind. 29 (May 2014) 13–21, https://doi.org/10.1016/j.jlp.2014.01.001.

[22] N.P. Lebedeva, et al., Amount of free liquid electrolyte in commercial large format prismatic Li-ion battery cells, J. Electrochem. Soc. 166 (4) (2019) A779–A786, https://doi.org/10.1149/2.1151904jes.

[23] F. Ferrario, S. Hildebrand, R. da Costa Barata, M. Lazareanu, N. Lebedeva, V. Busini, Li-ion battery electrolyte vapour cloud dispersion: an experimental and computational fluid dynamics approach, in: presented at the 37th Topical Meeting of the International Society of Electrochemistry, Stresa,Italy, Sep. 06, 2024 [Online]. Available: https://topical37.ise-online.org/.

[24] E. Bormashenko, A. Musin, R. Pogreb, E. Luz, M. Zinigrad, Thickness of gravity-flattened water layers (‘puddles’) deposited on the polymer substrates and the hysteresis of the contact angle, Colloids Surf. Physicochem. Eng. Asp. 372 (1–3) (Dec. 2010) 135–138, https://doi.org/10.1016/j.colsurfa.2010.10.002.

[25] B. Adrià Mora, M. Hilpert, Differences in infiltration and evaporation of diesel and gasoline droplets spilled onto concrete pavement, Sustainability 9 (7) (Jul. 2017) 1271, https://doi.org/10.3390/su9071271.

[26] F. Wang, J. Wu, Z. Liu, Surface tensions of mixtures of diesel oil or gasoline and dimethoxymethane, dimethyl carbonate, or ethanol, Energy Fuels 20 (6) (Nov. 2006) 2471–2474, https://doi.org/10.1021/ef060231c.

[27] G. Zhao, S. Bi, X. Li, J. Wu, Surface tension of diethyl carbonate, 1,2-dimethoxyethane and diethyl adipate, Fluid Phase Equilib 295 (1) (Aug. 2010) 46–49, https://doi.org/10.1016/j.fluid.2010.03.040.

[28] Y. Sun, C.J. Radke, B.D. McCloskey, J.M. Prausnitz, Wetting behavior of four polar organic solvents containing one of three lithium salts on a lithium-ion-battery separator, J. Colloid Interface Sci. 529 (Nov. 2018) 582–587, https://doi.org/10.1016/j.jcis.2018.06.044.

[29] B. Dollet, F. Boulogne, Natural convection above circular disks of evaporating liquids, Phys. Rev. Fluids 2 (5) (May 2017) 053501, https://doi.org/10.1103/PhysRevFluids.2.053501.

[30] B. Seo, Y. Wang, Experimental measurement of molecular diffusion and evaporation rate of battery organic electrolytes in ambient air, J. Electrochem. Soc. 168 (6) (Jun. 2021) 060505, https://doi.org/10.1149/1945-7111/ac0551.

[31] R.H. Perry, D.W. Green (Eds.), Perry’s Chemical engineers’ Handbook, 8. ed., McGraw-Hill, New York, NY, 2008.

[32] Y. Li, G. Liu, Z. Li, Numerical modeling of thermal runaway in high-energy lithium-ion battery packs induced by multipoint heating, Case Stud. Therm. Eng. 38 (Oct. 2022) 102335, https://doi.org/10.1016/j.csite.2022.102335.

[33] C.J.H. van den Bosch, R.A.P.M. Weterings, Methods for the calculation of physical effects: due to releases of hazardous materials, liquids and gases : yellow Book. Publicatiereeks Gevaarlijke stoffen. Ministerie van Volkshuisvesting en Ruimtelijke Ordening (VROM), 2005 [Online]. Available: https://books.google.it/books?id=v4iEnQAACAAJ.

[34] R.J. Goldstein, E.M. Sparrow, D.C. Jones, Natural convection mass transfer adjacent to horizontal plates, Int. J. Heat Mass Transf. 16 (5) (May 1973) 1025–1035, https://doi.org/10.1016/0017-9310(73)90041-0.

[35] B. Liu, X. Liu, C. Lu, A. Godbole, G. Michal, A.K. Tieu, Computational fluid dynamics simulation of carbon dioxide dispersion in a complex environment, J. Loss Prev. Process Ind. 40 (Mar. 2016) 419–432, https://doi.org/10.1016/j.jlp.2016.01.017.

[36] N. O. of D. and Informatics, “Carbonic acid, dimethyl ester.” Accessed: Apr. 21, 2025. [Online]. Available: https://webbook.nist.gov/cgi/cbook.cgi?ID=C616386&Mask=200.

[37] N. O. of D. and Informatics, “Diethyl carbonate.” Accessed: Nov. 18, 2024. [Online]. Available: https://webbook.nist.gov/cgi/inchi?ID=C105588&Mask=200.

[38] V. Pokorný, V. Štejfa, M. Fulem, C. Červinka, K. Růžička, Vapor pressures and thermophysical properties of dimethyl carbonate, diethyl carbonate, and dipropyl carbonate, J. Chem. Eng. Data 62 (10) (Oct. 2017) 3206–3215, https://doi.org/10.1021/acs.jced.7b00295.

[39] S.A. Kozlova, et al., Vapour pressure and enthalpy of vaporization of aliphatic dialkyl carbonates, J. Chem. Thermodyn. 40 (7) (Jul. 2008) 1136–1140, https://doi.org/10.1016/j.jct.2008.02.012.

[40] Y. Zhou, J. Wu, E.W. Lemmon, Thermodynamic properties of dimethyl carbonate, J. Phys. Chem. Ref. Data 40 (4) (Dec. 2011) 043106, https://doi.org/10.1063/1.3664084.

[41] B.E. Poling, J.M. Prausnitz, J.P. O’Connell, The Properties of Gases and Liquids, 5th ed., McGraw-Hill, New York, 2001.

[42] X. Zhang, J. Zuo, C. Jian, Experimental isobaric vapor−liquid equilibrium for binary systems of ethyl methyl carbonate + methanol, + ethanol, + dimethyl carbonate, or + diethyl carbonate at 101.3 kPa, J. Chem. Eng. Data 55 (11) (Nov. 2010) 4896–4902, https://doi.org/10.1021/je100494z.

[43] P. Qin, A. Ricci, B. Blocken, CFD simulation of aerodynamic forces on the DrivAer car model: impact of computational parameters, J. Wind Eng. Ind. Aerodyn. 248 (May 2024) 105711, https://doi.org/10.1016/j.jweia.2024.105711.

[44] U.S. Department of Energy, “Dimethyl carbonate.” Accessed: Feb. 18, 2026. [Online]. Available: https://emhub1.energy.gov/pacteel/search#616-38-6.

[45] U.S. Department of Energy, “Diethyl Cabonate.” Accessed: Feb. 18, 2026. [Online]. Available: https://emhub1.energy.gov/pacteel/search#105-58-8.